

Self-Assembled Ag–TiN Hybrid Plasmonic Metamaterial: Tailorable Tilted Nanopillar and Optical Properties

Xuejing Wang, Jie Jian, Zhiguang Zhou, Cuncai Fan, Yaomin Dai, Leigang Li, Jijie Huang, Jianing Sun, Andrea Donohue, Peter Bermel, Xinghang Zhang, Hou-Tong Chen, and Haiyan Wang*

Key challenges limiting the adoption of metallic plasmonic nanostructures for practical devices include structural stability and the ease of large-scale fabrication. Overcoming these issues may require novel metamaterial fabrication with potentials for improved durability under extreme conditions. Here, a self-assembled growth of a hybrid plasmonic metamaterial in thin-film form is reported, with epitaxial Ag nanopillars embedded in TiN, a mechanically strong and chemically inert matrix. One of the key achievements lies in the successful control of the tilt angle of the Ag nanopillars (from 0° to 50°), which is attributed to the interplay between the growth kinetics and thermodynamics during deposition. Such an anisotropic nature offered by the tilted Ag nanopillars in TiN matrix is crucial for achieving broadband, asymmetric optical selectivity. Optical spectra coupled with numerical simulations demonstrate strong plasmonic resonance, as well as angular selectivity in a broad UV–vis to near-infrared regime. The nanostructured metamaterials in this work, which consist of highly conductive metallic nanopillars in a durable nitride matrix, have the potential to serve as a novel hybrid material platform for highly tailorable nanoscale metamaterial designs, suitable for high temperature optical applications.

as “nanoantenna” for highly sensitive energy harvesting, photodetection, or light selectivity in terms of angular, frequency, or polarization.^[15–18] From the material perspective, metal-based plasmonic and optical nanostructures (gold (Au), silver (Ag), aluminum (Al) and copper (Cu)) have drawn a great deal of attention because of their strong surface-enhanced Raman scattering (SERS) and surface plasmon modes, which range from visible to near-infrared.^[11,19–22] Variable patterned nanoresonators (e.g., nanoprisms, nanorods, nanohole arrays, and single nanoparticle) have been demonstrated for improved resolution and signal-to-noise ratios for localized surface plasmon resonance (LSPR) spectroscopy.^[23–28]

In parallel, challenges remain in the plasmonic metamaterials, namely long-term durability and ease of fabrication. On one hand, metals such as Ag, Al, and Cu experience poor thermal stability and

fast chemical reactions upon thermal fluctuations. Furthermore, potential interdiffusion at metal–matrix (i.e., oxides, semiconductor) interface deteriorates device sensitivity at high temperatures.^[24,29,30] One effective approach is the design of hybrid plasmonic nanostructures such that the unstable phase can be embedded or covered with a durable material. Examples such as Ag/Au core-shell nanoparticles, Ag/AgS₂ nanoprisms, or Ag/graphene fishnet hybrids have been designed to enhance the overall stability and signal-to-noise ratios of SERS signals.^[24,29,31–33] On the other hand, existing metamaterial fabrication techniques such as e-beam lithography or focused

1. Introduction

Metamaterials as plasmonic nanoresonators with novel functionalities are attractive for various device applications including nanophotonic circuits, biomedical sensing, plasmon-enhanced photocatalysis, and photovoltaics.^[1–14] Through tailoring material or/and geometrical parameters of such nanostructured building blocks, light–matter interactions can be manipulated for selective responses. From geometrical perspective, nanopillar or nanowire becomes favorable candidate owing to their 3D tunability and optical anisotropy, which functions

X. Wang, Dr. J. Jian, C. Fan, Dr. L. Li, Dr. J. Huang, Prof. X. Zhang, Prof. H. Wang
Department of Materials Engineering
Purdue University
West Lafayette, IN 47907, USA
E-mail: hwang00@purdue.edu
Z. Zhou, Prof. P. Bermel
Birck Nanotechnology Center
Purdue University
West Lafayette, IN 47907, USA

Dr. Y. Dai, Dr. H.-T. Chen
Center for Integrated Nanotechnologies
Materials Physics and Applications Division
Los Alamos National Laboratory
Los Alamos, NM 87545, USA

J. Sun, A. Donohue
J.A. Woollam Co. Inc.
645 M Street, STE 102, Lincoln, NE 68508, USA

Prof. H. Wang
Department of Electrical and Computer Engineering
Purdue University
West Lafayette, IN 47907, USA

 The ORCID identification number(s) for the author(s) of this article can be found under <https://doi.org/10.1002/adom.201801180>.

DOI: 10.1002/adom.201801180

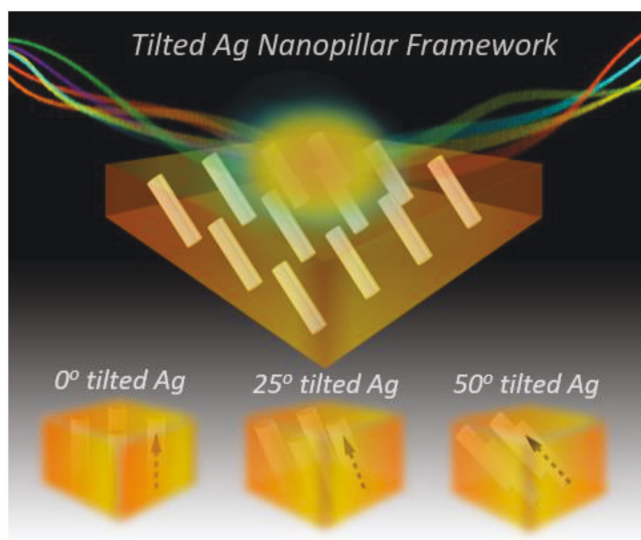


Figure 1. Schematic illustration of Ag–nitride (TiN) hybrid plasmonic metamaterial thin film. Ag nanopillars with subwavelength scale are tailored in terms of their tilting angles (lower pane). The hybrid plasmonic configuration brings new functionalities such as optical anisotropy and angular selectivity.

ion-beam techniques are time consuming for nanoscale geometries. Beam damage and limited patterning scale are also concerns to the fabrication of high-quality and large-scale photonic devices. Alternative methods such as anodized alumina template and seeded growth are capable of producing epitaxial nanopillars/nanoparticles, but have limitations in material and morphology selections.^[2,34–36] Recent demonstrations on the two-phase nanocomposite growth using physical vapor deposition techniques open up more possibilities in fabricating high-quality, large-scale metamaterials.^[37]

In this work, we report a novel nanoscale metamaterial system that composes of tilted Ag nanopillars in a titanium nitride (TiN) matrix, grown as hybrid thin-film form. The 3D Ag–TiN framework is illustrated in **Figure 1**. Here, we highlight the structural tunability in terms of pillar tilting angle, which can be tailored by precise growth control. Different from oblique angle deposition, which produces mostly single-phase tilted nanorods,^[3,38,39] this one-step deposition method achieves the self-assembly of two-phase hybrid materials with high epitaxial quality and high-density nanopillar assemblies approaching deep subwavelength scale (<10 nm), which is very challenging for the current fabrication techniques. Such tilted geometry presents enormous opportunities in achieving optical anisotropy and angular selectivity. In addition, compared to patterned metallic nanostructure or metasurfaces,^[3,30,36] the robust TiN matrix serves as a barrier against diffusion and surface chemical reaction for Ag, and provides overall mechanical integrity. Detailed studies of the physical properties have been performed, which include specular reflectance and dielectric measurements from ultraviolet (UV) to infrared (IR) regime, thermal and mechanical tests, along with a complete microstructural analysis to correlate the optical responses with the tilted Ag nanopillar geometries.

2. Results and Discussion

A set of Ag–TiN hybrid thin films were deposited following the structure designs as illustrated in **Figure 1**, where the embedded Ag nanopillars are tilted I) 0°, II) 25°, and III) 50°, respectively. Such tilting is achieved by precision growth control discussed below. To confirm the tilting pillars and the overall film morphology, plan-view transmission electron microscopy (TEM) study was conducted and the images are presented in **Figure 2a–c** for all three samples. Upon increasing the tilt angle from 0° to 50°, the top projections of Ag nanopillar assemblies change from round to elongated shapes. With comparable Ag densities controlled for all samples, the metasurface affected by Ag tilting geometries could effectively change the surface plasmonic resonances, to be discussed in later sections. The corresponding cross-sectional scanning transmission electron microscope (STEM) images of different tilting configurations are shown in **Figure 2d–f**, in which distinct Ag nanopillars are clearly identified with a uniform distribution and tilt angle for each case. Selected area electron diffraction (SAED) patterns taken from the <100> zone axis (inset images) confirm high-quality epitaxy, as well as a cube-on-cube matching of (002) atomic planes of Ag and TiN on magnesium oxide (MgO) substrates. Energy-dispersive X-ray spectroscopy (EDS) mappings of Ti (green) and Ag (red) are shown as insets in **Figure 2d,f**, which clearly confirm the growth of Ag nanopillars in a TiN matrix with very clean interfaces and without obvious intermixing. Based on the (S)TEM results, detailed quantifications including nanopillar dimensions and tilting angles are summarized in the Supporting Information, which correlated to three deposition rates. Results indicate that lower deposition rate increases the tilting angle and broadens the nanopillar dimension slightly, meanwhile the nanopillar lengths remain comparable even though the overall film thickness is reduced.

In parallel, X-ray diffraction (XRD) was collected to confirm the film crystallinity from a large area. The θ – 2θ scans of three hybrid films and a pure TiN film are shown in **Figure S1** in the Supporting Information. The growth orientation is identified as (002) Ag || (002) TiN || (002) MgO for the Ag–TiN hybrid films. Peak positions are identified as $2\theta_{\text{TiN}} = 42.60^\circ$, $2\theta_{\text{Ag}} = 44.283^\circ$, and $2\theta_{\text{MgO}} = 42.916^\circ$, which match well with all the peak positions of the bulk counterparts. Close lattice matching between MgO ($a_{\text{MgO}} = 0.421$ nm) substrate and TiN ($a_{\text{TiN}} = 0.424$ nm) provides a desired epitaxial template for the growth of Ag nanopillars, evidenced by the dominated Ag (00 l) peaks without any other orientations. Compared to pure TiN, the two-phase heteroepitaxial Ag–TiN results in a slightly broadened (002) TiN peak, which could be related to the vertical coupling at Ag/TiN interface or minor variations on TiN stoichiometry at the interfaces. Overall, the films maintain high quality and very smooth surface as seen from the satellite peaks of (002) TiN. A ϕ (φ) scan of Ag–TiN hybrid film (**Figure S1b**, Supporting Information) demonstrates a fourfold symmetry of the film, and excellent in-plane alignment, with cube-on-cube matching for all the phases. Successful tilted growth of Ag–TiN hybrid film is also achieved on c-cut sapphire substrate, with the growth orientation as (111) Ag || (111) TiN || (0001) sapphire based on XRD (**Figure S1c**, Supporting Information). The corresponding STEM images (**Figure S1d**, Supporting Information)

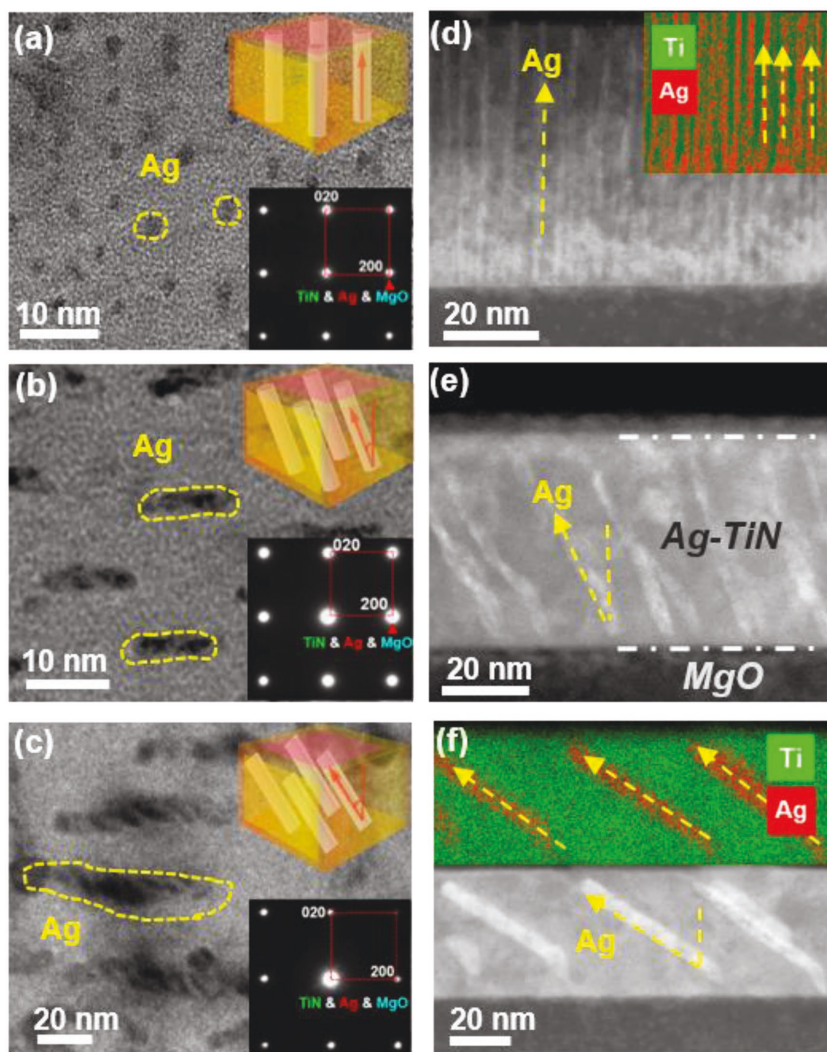


Figure 2. 3D morphology of epitaxial Ag–TiN hybrid thin films with different nanopillar tilting geometries. a–c) Plan-view TEM images of 0° tilted, 25° tilted, and 50° tilted Ag. d–f) Cross-sectional SAED images corresponding to each geometry. Insets are selected area electron diffraction (SAED) patterns taken at $\langle 100 \rangle$ zone axis, as well as EDS mapping of two extreme angles. Ag is mapped in red and Ti is mapped in green.

demonstrate well-ordered nanopillar assembly achieved on sapphire substrate as compared to films grown on MgO substrate.

Both (S)TEM and XRD results confirm the preferred growth orientation of (002) Ag nanopillars. To explore the growth mechanism for the tilted nanopillars, high-resolution STEM was performed on the 50° tilted Ag–TiN/MgO hybrid film from three dimensions, as illustrated in Figure 3 (top center). Cross-sectional STEM images taken from the $\langle 100 \rangle$ zone axis are shown in Figure 3a,b. The Ag nanopillars growth experiences two steps: the initial nucleation (marked in the yellow box in Figure 3a) and the subsequent tilted growth. For the first few atomic layers, Ag adatoms stack vertically on top of each other. After the initial nucleation, the Ag adatoms continuously shift to the left while maintaining the (002) atomic stacking along the c -direction, resulting in the tilted nanopillar morphology. Inversed Fourier transformed images (Figure 3c,d) of Ag/TiN phase boundary indicate strained interface with few misfit

dislocations along in-plane and out-of-plane directions, which is also proven by the atomic resolution Ag/TiN from the top projection (Figure 3e). When viewed from the orthogonal $\langle 010 \rangle$ zone axis (Figure 3f), the nanopillars appear to be mostly vertically aligned. Minor contrast variations across the length of the Ag nanopillar indicate the “vertical pillar” is tilted inward, which is in the projection of [010] as illustrated. Therefore, the self-assembled 50° Ag nanopillar assembly has been demonstrated from a 3D perspective.

The underlying mechanism of this self-assembled tilting geometry is attributed to the competition between growth kinetics and thermodynamics. On one hand, high kinetic energy of pulsed laser deposition (PLD) method allows fast thin-film deposition and facilitates the Ag nanopillars to grow vertically along the primary growth direction. With a nearly perfect lattice matching between TiN and MgO, Ag prefers to grow as epitaxial (00l). Such pillar-in-matrix nanostructures are realized by the difference in surface energies, i.e., Ag has higher surface energy and thus nucleates in the Volmer–Weber island growth mode, and TiN nucleates as Stranski–Krastranov (2D + 3D) mode, both on oxides.^[40] Under a high growth rate (upper pane of Figure S2, Supporting Information), the Ag and TiN adatoms grow and nucleate effectively as vertical columns with limited time for adatom diffusion on the substrate surface, leading to vertically aligned nanopillars. Thus, Ag nucleus appears fine and densely packed as observed from Figure 2a. On the other hand, when the growth rate reduces (lower pane of Figure S2, Supporting Information), the adatom diffusion along the lateral direction is enabled by a longer resting time, searching for a thermodynamically favorable state of growth;

thus, larger nuclei and lateral tilting of the pillars become possible. Here, the growth of the hybrid Ag–TiN film starts from a thin layer of TiN to minimize the lattice mismatch strain in the initial growth stage, considering the nearly perfect matching between TiN and MgO substrate. Thus, a very thin layer of TiN (1–4 nm) is formed at the interface. It is noted that the initial TiN layer thickness is affected by overall growth rate as well, i.e., under a low rate, this layer tends to grow thicker before the Ag adatoms diffuse and form stable nucleus. After the initial nucleation process, the TiN growth is suppressed by the tilted growth of Ag nanopillars, leading to an overall thinner film as compared to the higher deposition rate ones. Comparing the surface energies of different Ag crystallographic planes, (111) is the lowest among (100), (110), and (111).^[41] This low-energy plane has the tendency to be exposed to minimize surface energy for low growth rates, which in turn results in tilted growth that remains the [001] stacking orientation. While the

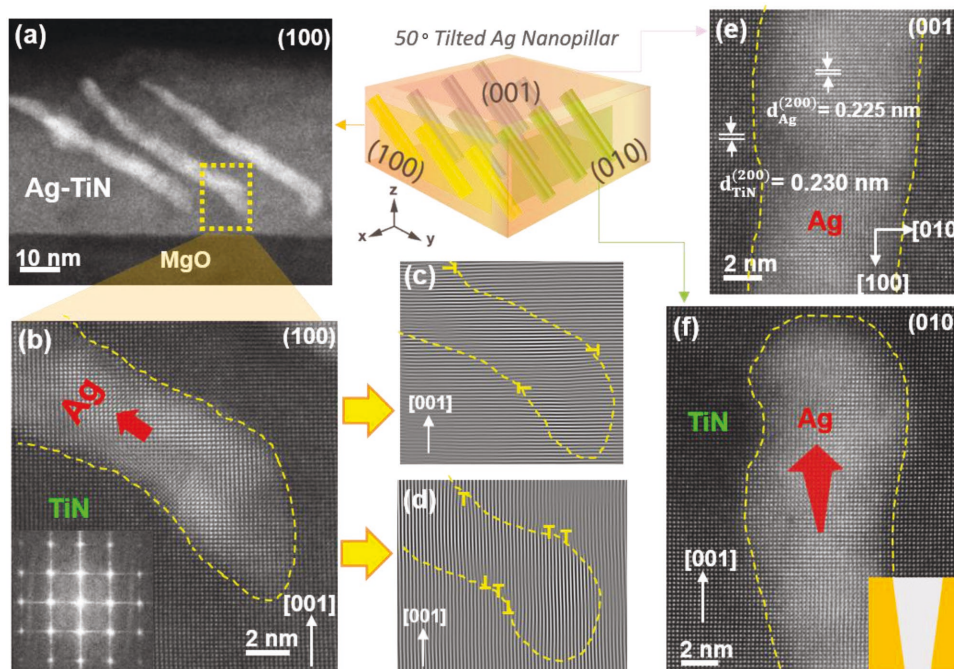


Figure 3. STEM images of 50° Ag–TiN hybrid thin film. Schematic illustration is shown at top center showing three faces (100), (010), and (001). a) Cross-sectional STEM and b) its high magnification image, taken at $\langle 100 \rangle$ zone axis, (100) face. c,d) Inverted Fourier transform image both out-of-plane and in-plane with misfit dislocations marked at Ag/TiN interface. e) HRSTEM image of plan-view (001) face) nanopillar. f) Cross-sectional HRSTEM image taken from $\langle 010 \rangle$ zone axis, showing projection of one tilted nanopillar from [010] direction.

overall kinetic energy is largely determined by the laser energy, the degree of tilting is primarily controlled by fine tuning of the parameters affecting deposition rate. Compared with 0° and 25° tilting geometry shown in Figure 2, the 50° tilting reaches to a relative thermodynamic stable state. Note that the inhomogeneity in the hybrid materials (i.e., nanopillar diameter, nucleus density) is inevitable when tailoring the tilting angle parameters. In this study, the optical property is mainly focused on the angular-dependent (anisotropic) light–matter interactions such that the dimension effect can be minimized.

Optical measurements on Ag–TiN hybrid thin films demonstrate a variable spectrum response by tailoring the Ag nanopillar geometry. Optical reflectance and transmittance spectra of pure TiN, and 0° tilted and 50° tilted Ag–TiN thin-film samples were collected under a normal incident depolarized light. The absorbance spectrum is retrieved from reflectance as $A(\lambda) = 1 - R(\lambda)$, since transmittance is negligible, and a Lorentz function is applied to split the peaks. The results are shown in Figure 4a. Pure TiN film (85 nm) (in gray curve) exhibits plasmonic behavior, with an absorbance peak located at 374 nm. For Ag–TiN hybrid structures (blue and orange curves), two separate peaks are noted. To correlate the peak positions of the two phases, COMSOL Multiphysics Wave Optics Module was applied to simulate the optical spectra and the corresponding electric field map. Parameters such as film thickness, pillar dimension, as well as the interpillar distance are comparable to (S)TEM results. In order to identify peak positions, pure Ag and TiN spectra were simulated individually, from which it is confirmed that the left (≈ 350 nm) and right (≈ 374 nm) resonance peak (Figure 4a) belongs to Ag and TiN phase, respectively. A careful

comparison on peak positions reveals a red shift (40 nm) of TiN resonance peak, which is related to a minor change in TiN stoichiometry or defect states at Ag/TiN interface. Variations of Ag resonance peak positions (330–350 nm) are attributed to the change of nanopillar aspect ratio, while intensity variation is caused by light propagation direction with respect to nanopillar tilting direction. It can be explained by stronger electron oscillations at the resonant frequency when the incident light propagates into the vertically aligned nanopillar, or LSPR at the Ag/TiN interfaces. Compared to pure TiN, Ag–TiN hybrid film presents a broadened absorbance (Figure 4a); such increase of linewidths lies in the superposition of two-phase plasmonic resonances, which implies enhanced electron oscillation and stronger near-field coupling upon electromagnetic field excitation. It also could be attributed to the possible variations in material composition, interfacial strains, and degree of ordering of nanopillars. A general enhancement of the baseline intensity results from scattering at interfaces or defects. Next, the field enhancement maps are retrieved close to the resonant frequencies of two phases and displayed in Figure 4b. At 350 nm, electrical field of γ -polarization (E_y) is dominated by Ag nanopillars, while the TiN excitation is maximized at 420 nm. Additionally, the 0° tilted Ag nanopillar reveals more centrosymmetric electric field distribution, while it becomes more anisotropic when the nanopillar is tilted. Such field distribution inside tilted geometries indicates potential angular selectivity when the light is propagating along different directions. The non-centrosymmetric or anisotropic nature of this nanostructure is further proved by the second harmonic generation (SHG) (Figure 4c). The polar plot indicates a transition

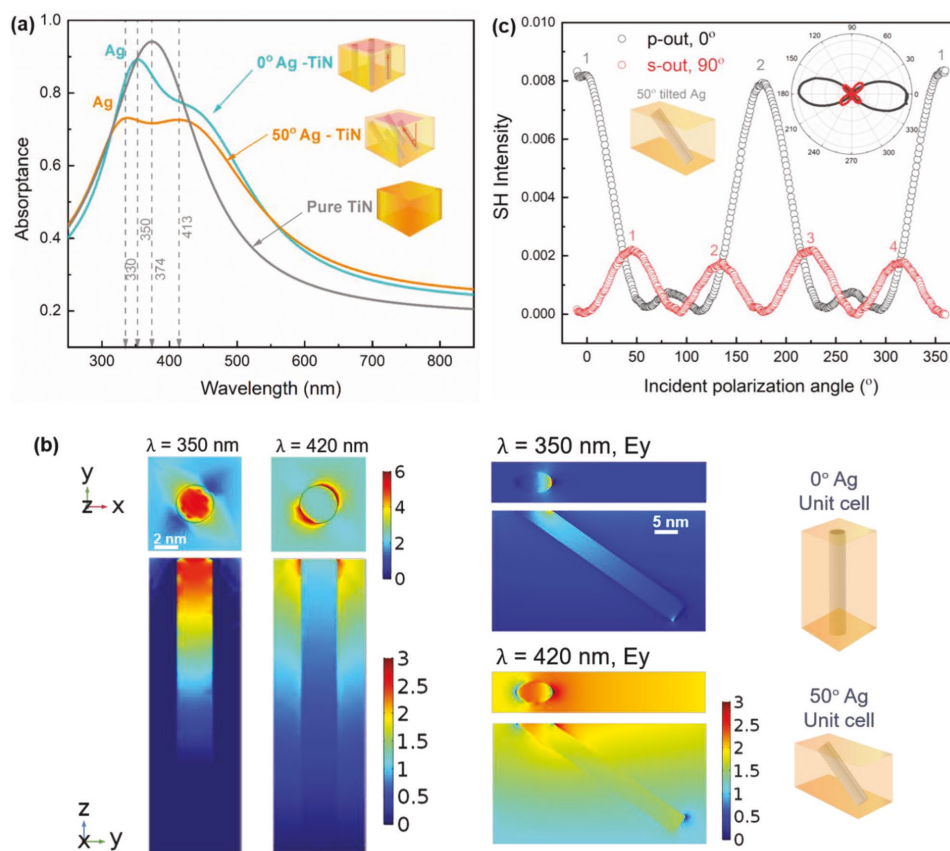


Figure 4. Optical properties in the UV-vis range. a) Absorbance spectra of pure TiN, 0° tilted Ag-TiN, and 50° tilted Ag-TiN hybrid thin films. Two peaks observed at 330–350 nm and 374 nm correspond to Ag SPR and TiN signals. b) 2D electric field (E_y) distribution on 0° tilted Ag-TiN and 50° tilted Ag-TiN hybrid films close to resonant frequencies (350 and 420 nm). Models are built based on the corresponding geometries, normal incident depolarized beam is applied. Details on simulation are described in the Experimental Section. c) Second harmonic (SH) signals of 50° tilted Ag-TiN hybrid film, collected from p- and s-output polarizations, inset is the polar plot of SH intensity.

from a twofold rotational symmetry at p-out (0°) to a fourfold symmetry at s-out (90°) with decreased SHG intensity. Such non-centrosymmetric nature of the sample could be attributed to the anisotropic tilted Ag nanopillars, the lattice strain coupling between TiN and Ag nanopillars, and the strain between the film and substrate. Based on XRD data (Figure S1, Supporting Information), it is obvious that TiN and Ag are under compressive and tensile strain out-of-plane, respectively, due to the strong interface coupling between TiN and the Ag pillars. Such strain induces lattice distortion of both phases during thin-film growth, which breaks the centrosymmetry from their bulk counterparts and contributes to SHG signals. Such SHG signals have been previously reported in metallic thin films.^[42]

To demonstrate potential angular selectivity (anisotropy) over a wide spectral range, detailed ellipsometry and Fourier transform infrared (FTIR) spectroscopy measurements have been performed. Nonpolarized angular reflectance at 210–2500 nm range of 0° Ag-TiN and 50° tilted Ag-TiN thin films with thickness of 45 nm are retrieved from ellipsometry data and summarized in **Figure 5**. Since the tilt of Ag nanopillars breaks the symmetry along the normal incidence, it is important to differentiate incident beams with respect to the direction of nanopillars. For the sake of convenience, we use

the following convention: 1) when the light propagates along tilted nanopillars (or [010] direction), as shown in Figure 5a, the incident angles are positive (30°–70°) and 2) when light propagates in the opposite direction ([0 $\bar{1}$ 0] direction), as shown in Figure 5b, the incident angles are negative (from –30° to –70°). For positive angles of incidence, the overall reflectance drops with increased incident angles due to the enhanced localized plasmonic resonance along the nanopillar interface, reaching a more pronounced dip ($\approx 10\%$) at 400 nm. For negative angles of incidence, however, the reflection is stronger throughout the spectrum range, while the dropped reflectance at higher angles ($\alpha \leq -60^\circ$) could be caused by internal reflection as light propagates inside the film. The above explanation is supported by the simulated E_y maps (Figure 5e), where obvious interface resonance is observed at positive angle excitations (along nanopillar), while enhanced reflectance from Ag nanopillar and metasurface is observed at negative angle excitations. As a comparison, while the reflectance from two propagating directions show similar trend in 0° Ag-TiN film (Figure 5c,d) with centrosymmetric distribution of electric field (see Figure S3, Supporting Information), it is certified that the 50° Ag-TiN hybrid film exhibits strong optical anisotropy that is sensitive to the direction of incoming light. In addition, the effective refractive

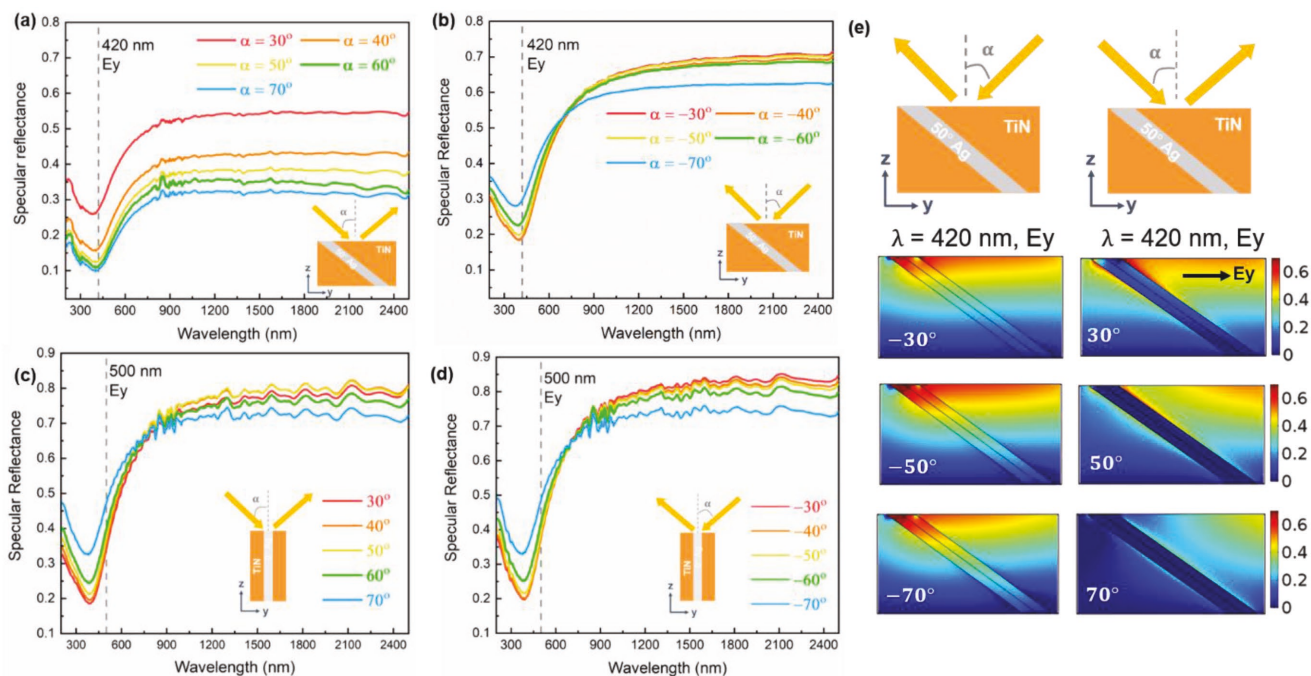


Figure 5. Angular dependent specular reflectance of two Ag–TiN hybrid films with 0° and 50° tilt. Five incidence angles (30°–70°) and wavelength of 210–2500 nm were covered. Two sets of data with 180° apart were measured as illustrated in the inset images. a,b) Specular reflectance from 50° Ag–TiN film. c,d) Specular reflectance from 0° Ag–TiN film. e) Electrical field maps at 420 nm of the 50° Ag–TiN film. Results demonstrate pronounced angular selectivity from the 50° tilted Ag nanopillar geometry when light propagates from opposite orientations.

index and permittivity of the 50° tilted Ag–TiN and a pure TiN are fitted using a B-Spline model, shown in Figure S4 in the Supporting Information. The slight decrease in the extinction coefficient indicates lower losses in this wavelength range for the Ag–TiN hybrid sample. Besides, the hybrid films show a pronounced dielectric tuning toward the infrared regime, i.e., plasma frequency shift, and change of conductivity, which is evidenced from the temperature dependent resistivity (R - T) via the electrical transport property measurement (Figure S5, Supporting Information).

In the longer wavelength regime (2–10 μm), specular reflectance of the 50° Ag–TiN film was measured by FTIR. Here, the propagation directions of light follow the convention of the sign of angles as described above, where incident angles are set to be $\alpha = 30^\circ$ – 70° and $\alpha = -30^\circ$ to -70° with respect to the pillar geometry. To visualize the angular-dependent reflectance, spectra along y - z plane are plotted together with polar plots of reflectance at four arbitrary wavelengths ($\lambda = 2, 3, 5, 8 \mu\text{m}$), as shown in Figure 6c. It is noted that the asymmetry of the polar plot becomes more pronounced toward short-wavelength IR. The reflectance reaches its maximum around $\alpha = -30^\circ$ throughout the spectrum (red arrows). Such trend is observed at the visible range as well (Figure 5b). Combining the illustration, the angular selectivity or anisotropic behavior of the hybrid film is dominated by tilted nanopillar especially at lower incident angles and shorter wavelengths (2–5 μm). It is noted that the angular selectivity in this work is modest, but much higher selectivity is expected with improved periodicity and ordering of the nanopillars, which are currently under investigation. Highly angular-selective hybrid films are expected to

find promising applications as functional nanoantennas, sensors, and related applications.

Metamaterial stability is critical for device applications. Here, a highly stable hybrid nanostructure is achieved by applying TiN as the matrix to encapsulate Ag nanopillars. To test the thermal stability, an as-deposited Ag–TiN sample (grown on MgO) was annealed at 500 °C for 1 h under vacuum, followed by ex situ optical and XRD measurements as shown in Figure S6a,b in the Supporting Information. Neither peak-shifting nor broadening has been observed, which indicates excellent phase stability after heat treatment. Furthermore, thermal emissivity measurements provide more evidence of high-temperature stability at the infrared range. The measurement was performed in a high-vacuum chamber coupled with an FTIR spectrometer.^[43] Three spectra collected at the sample (50° Ag–TiN grown on sapphire) temperatures of 432, 471, and 519 °C are shown in Figure S6c in the Supporting Information. Results demonstrate very stable emissivity within the temperature range, while the spectrum differs from that of the room-temperature one caused by the incident angles (within $\pm 32^\circ$). The nanopillars maintain their sharpness at submicron-sized interfaces without any interdiffusion or damage after the high-temperature measurements, as indicated in cross-sectional STEM images shown in Figure S6d in the Supporting Information. To test the mechanical stability, a set of nanoindentation experiments was performed on thick TiN (1 μm) and Ag–TiN (600 nm) hybrid films grown on MgO. TiN is known as a refractory coating material with superior hardness ($H_{\text{TiN}} = 23$ – 25 GPa) compared to relatively soft noble metals ($H_{\text{Au}} = 188$ – 216 MPa , $H_{\text{Ag}} = 250 \text{ MPa}$). Figure S7 in the Supporting Information displays the typical loading–unloading

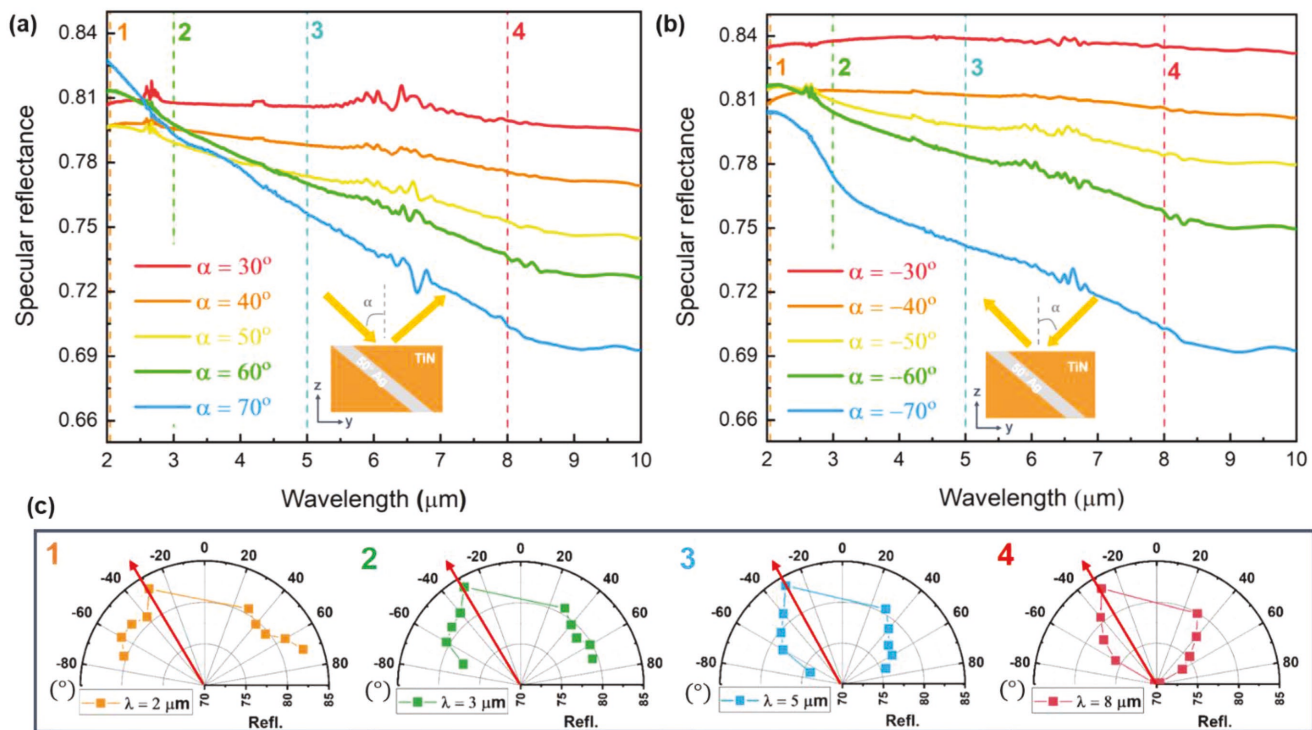


Figure 6. Room temperature specular reflectance of 50° tilted Ag–TiN hybrid film. FTIR reflectance spectra grouped by incident light propagating a) along nanopillar tilting direction ([010]) and b) backside of nanopillar ($[0\bar{1}0]$), inset images show incident light direction from the cross-sectional view of unit cell. c) Polar plot showing reflectance intensities versus incident angles at four wavelengths: $2 \mu\text{m}$ (orange), $3 \mu\text{m}$ (green), $5 \mu\text{m}$ (blue), and $8 \mu\text{m}$ (red).

plots on indent distance (h_c) versus hardness (H) and Elastic Modulus (E_r). Surprisingly, the averaged H and E_r values for Ag–TiN hybrid film ($H = 32 \text{ GPa}$, $E_r = 337 \text{ GPa}$) are comparable to pure TiN film ($H = 34 \text{ GPa}$, $E_r = 335 \text{ GPa}$) without obvious softening induced by the Ag nanopillars. As a comparison to other metallic nanostructures or metasurfaces,^[1,22,29] this hybrid Ag–nitride thin-film metamaterial is durable under thermal vibration, chemical reaction, or mechanical deformation. Such new hybrid material could play an important role in maintaining device performance in terms of signal-to-noise ratio or specular sensitivity. More interestingly, this metal–nitride hybrid platform provides enormous opportunities for realizing other nanoscale metal plasmonic structures in which thermal stability and long-term durability could be enhanced significantly.

3. Conclusion

In this work, self-assembled Ag–TiN nanoscale hybrid plasmonic thin films are demonstrated with tailorable Ag nanopillar tilting geometries and anisotropic optical properties. Distinguished nanopillars with high epitaxial quality are confirmed by XRD and (S)TEM studies. Tilting of Ag nanopillars is effectively controlled by film growth rate (or adatom flux), i.e., decreased deposition rate facilitates in-plane adatom diffusion and leads to thermodynamically favored tilted nanopillar growth. The Ag–TiN hybrid material shows strong absorption

in the visible regime, with contributions from both Ag and TiN SPRs phases and can be tuned by varying the tilting geometry. Tilted Ag nanopillars offer advantages such as enhanced electromagnetic interactions at nanopillar interfaces, strong anisotropic interactions with light and tunable dielectric constants, and obvious asymmetric angular selectivity based on the broadband reflectance data in the UV to mid-infrared regime. Combined with high thermal stability and enhanced mechanical integrity, such plasmonic metal–nitride hybrid nanostructures with structural and optical tunability present a promising and unique platform for novel nanoscale metamaterial design incorporating tailored angular and spectral selectivity, along with superior long-term structural durability.

4. Experimental Section

Sample Fabrication: Self-assembled hybrid Ag–TiN thin films were grown on single crystalline MgO (001) and c-cut sapphire ($\alpha\text{-Al}_2\text{O}_3$) substrates. Deposition was carried on a PLD system with KrF excimer laser (Lambda Physik Compex Pro 205, $\lambda = 248 \text{ nm}$, 5 Hz). The laser beam was focused onto the target with an incident angle of 45° and an energy density of around 3.0 J cm^{-2} . Ag foil piece was pasted with TiN target for two-phase deposition. The chamber was pumped to lower than $1.0 \times 10^{-6} \text{ mbar}$ to provide a desired vacuum deposition condition. Substrate temperature was maintained at $500\text{--}600^\circ \text{C}$. Deposition rate was controlled by substrate to target distance. After the deposition, the chamber was cooled to room temperature at $15^\circ \text{C min}^{-1}$ under vacuum.

Microstructure Characterization: The microstructures of the films were characterized by XRD and TEM, and STEM. XRD θ – 2θ scans were

performed using a Panalytical X'Pert X-ray diffractometer with Cu K_{α} radiation. Bright field TEM images, SAED patterns, and EDS chemical mapping were acquired by the FEI Talos F200X TEM. High-resolution STEM was carried on a modified FEI Titan microscope with an hexapole-type illumination aberration corrector. The TEM samples were prepared using a standard cross-section sample preparation procedure, including manual grinding, polishing, dimpling, and an ion milling step (PIPS 691 precision ion polishing system, 4.0 keV).

Optical Properties: Normal incident depolarized transmittance ($T\%$) and reflectivity ($R\%$) spectra were measured using an optical spectrophotometer (Lambda 1050 UV-vis Spectrophotometer) with integrated sphere detector and total absolute measurement system. Ellipsometry experiments were carried on an RC2 spectroscopic ellipsometer (J.A. Woollam Company). Three angles 30° , 45° , and 60° and a spectrum range from 210 to 2500 nm were covered for the measurements. SHGs were measured on an amplified Ti:sapphire laser system at room temperature with central wavelength of 780 nm, laser impinging power of 10 mW, and pulse duration of ≈ 70 fs. The polarization of the incident light was controlled by a half-wave plate and the SHG signal in the reflection from the sample with an angle of incidence at 45° was measured while with output polarization was fixed at either 0° (p-out) or 90° (s-out). Specular reflectance ($2\text{--}10\ \mu\text{m}$) at various angles of incidence were measured using Thermo Fisher Nexus 670 FTIR spectrometer and a specular reflectance accessory (VeeMax II, PIKE Technologies, Inc.). The reference for specular reflectance measurement was a 200 nm Au evaporated on glass slide with Ti adhesion layer. High-temperature emissivity was measured by a high vacuum chamber coupled with an FTIR spectrometer with a liquid nitrogen cooled mercury cadmium telluride detector and an XT-KBr beam splitter (Thermo Fisher Nexus 670). Details of high-temperature emissivity measurement could be found elsewhere.^[43]

Electrical Properties: The electrical resistivity of as-deposited films was measured by a standard four probe method with temperature varied from 5 to 390 K in a physical property measurement system (Quantum Design).

Mechanical Test: Nanoindentation experiment was performed on a Bruker Hysitron TI Premier instrument. A set of loading-unloading cycles were applied with changes on indent distance, which was controlled within 12% of film thickness to avoid substrate effect.

Simulation: COMSOL Multiphysics Wave Optics Module with frequency domain was applied for optical simulation. Optical constant for Ag was taken from Rakic,^[44] while refractive index for TiN was retrieved from ellipsometry measurements. The simulated geometry was based on the cross-sectional STEM images, including the film thickness, Ag tilting angles, nanopillar dimension, and the interpillar distance. The unit cell of hybrid film was set as one pillar in matrix with periodic boundaries, resulting in a perfect ordering of pillar-in-matrix geometry. A plane wave source with depolarized light of the electric field was applied. Angular dependent reflectivity ($R\%$) was simulated with changed incident angle (α) from 30° to 60° . Optical parameters (i.e., real and imaginary part of permittivity) were retrieved using the CompleteEase Software Package with film considered as a B-Spline layer (absorbing). The averaged mean square error of data fitting was 1.529, indicating a desired match between measurements and simulations.

Supporting Information

Supporting Information is available from the Wiley Online Library or from the author.

Acknowledgements

The manuscript was drafted by X.W. and H.W.. All authors contributed to editing of the manuscript. This work was partially supported by the College of Engineering Start-up Fund and Basil R. Turner Professorship

at Purdue University. The atomic scale TEM/STEM imaging effort was funded by the U.S. National Science Foundation (DMR-1565822). X.W. and H.W. acknowledge the support from the U.S. National Science Foundation (DMR-1809520). This work was performed, in part, at the Center for Integrated Nanotechnologies, a U.S. Department of Energy, Office of Basic Energy Sciences Nanoscale Science Research Center operated jointly by Los Alamos and Sandia National Laboratories. P.B. and Z.Z. acknowledge the support from the Office of Naval Research (ONR) NEPTUNE under Grant #N000014-15-1-2833. This project was conceived by H.W. and the experiments were designed by X.W. and H.W. X.W. conducted the thin-film deposition, XRD, TEM sample preparation and imaging, and optical measurements and simulations. J.J. contributed in high-resolution STEM imaging and plan-view TEM imaging. L.L. and J.H. contributed in target preparation and technical support on sample fabrication. Z.Z. performed room-temperature FTIR and high-temperature emissivity experiments under the supervision of P.B. C.F. conducted nanoindentation tests under the supervision of X.Z. J.S. and A.D. contributed to the ellipsometry measurements. Y.D. measured the second harmonic generation under the supervision of H.-T.C. The manuscript was drafted by X.W. and H.W. All authors contributed to editing of the manuscript.

Conflict of Interest

The authors declare no conflict of interest.

Keywords

angular selectivity, hybrid plasmonics, optical anisotropy, thermal stability, tilted Ag nanopillars

Received: August 29, 2018

Revised: October 24, 2018

Published online: December 3, 2018

- [1] P. K. Jain, S. Eustis, M. A. El-Sayed, *J. Phys. Chem. B* **2006**, *110*, 18243.
- [2] J. H. Gao, X. Z. Wu, Q. W. Li, S. Y. Du, F. Huang, L. Y. Liang, H. L. Zhang, F. Zhuge, H. T. Cao, Y. L. Song, *Adv. Mater.* **2017**, *29*, 8.
- [3] P. Zilio, M. Malerba, A. Toma, R. P. Zaccaria, A. Jacassi, F. De Angelis, *Nano Lett.* **2015**, *15*, 5200.
- [4] S. Lincic, P. Christopher, D. B. Ingram, *Nat. Mater.* **2011**, *10*, 911.
- [5] J. N. Anker, W. P. Hall, O. Lyandres, N. C. Shah, J. Zhao, R. P. Van Duyne, *Nat. Mater.* **2008**, *7*, 442.
- [6] H. A. Atwater, A. Polman, *Nat. Mater.* **2010**, *9*, 205.
- [7] R. B. Jiang, B. X. Li, C. H. Fang, J. F. Wang, *Adv. Mater.* **2014**, *26*, 5274.
- [8] Z. W. Liu, W. B. Hou, P. Pavaskar, M. Aykol, S. B. Cronin, *Nano Lett.* **2011**, *11*, 1111.
- [9] N. J. Halas, S. Lal, W. S. Chang, S. Link, P. Nordlander, *Chem. Rev.* **2011**, *111*, 3913.
- [10] L. Y. Lu, Z. Q. Luo, T. Xu, L. P. Yu, *Nano Lett.* **2013**, *13*, 59.
- [11] K. Aydin, V. E. Ferry, R. M. Briggs, H. A. Atwater, *Nat. Commun.* **2011**, *2*, 7.
- [12] C. M. Soukoulis, M. Wegener, *Nat. Photonics* **2011**, *5*, 523.
- [13] W. Lewandowski, M. Fruhnert, J. Mieczkowski, C. Rockstuhl, E. Gorecka, *Nat. Commun.* **2015**, *6*, 9.
- [14] N. Engheta, *Science* **2007**, *317*, 1698.
- [15] Y. C. Shen, D. X. Ye, I. Celanovic, S. G. Johnson, J. D. Joannopoulos, M. Soljacic, *Science* **2014**, *343*, 1499.
- [16] Y. C. Shen, C. W. Hsu, Y. X. Yeng, J. D. Joannopoulos, M. Soljacic, *Appl. Phys. Rev.* **2016**, *3*, 011103.

- [17] T. Shegai, S. Chen, V. D. Miljkovic, G. Zengin, P. Johansson, M. Kall, *Nat. Commun.* **2011**, 2, 6.
- [18] J. Lin, J. P. B. Mueller, Q. Wang, G. H. Yuan, N. Antoniou, X. C. Yuan, F. Capasso, *Science* **2013**, 340, 331.
- [19] K. S. Lee, M. A. El-Sayed, *J. Phys. Chem. B* **2006**, 110, 19220.
- [20] M. Rycenga, C. M. Cobley, J. Zeng, W. Y. Li, C. H. Moran, Q. Zhang, D. Qin, Y. N. Xia, *Chem. Rev.* **2011**, 111, 3669.
- [21] H. R. Stuart, D. G. Hall, *Appl. Phys. Lett.* **1998**, 73, 3815.
- [22] A. Jakob, C. Rosman, Y. Khalavka, J. Becker, A. Trugler, U. Hohenester, C. Sonnichsen, *ACS Nano* **2011**, 5, 6880.
- [23] A. B. Dahlin, J. O. Tegenfeldt, F. Hook, *Anal. Chem.* **2006**, 78, 4416.
- [24] C. Xue, X. Chen, S. J. Hurst, C. A. Mirkin, *Adv. Mater.* **2007**, 19, 4071.
- [25] E. M. Hicks, X. Y. Zhang, S. L. Zou, O. Lyandres, K. G. Spears, G. C. Schatz, R. P. Van Duyne, *J. Phys. Chem. B* **2005**, 109, 22351.
- [26] A. D. McFarland, R. P. Van Duyne, *Nano Lett.* **2003**, 3, 1057.
- [27] X. M. Qian, S. M. Nie, *Chem. Soc. Rev.* **2008**, 37, 912.
- [28] N. F. Yu, F. Capasso, *Nat. Mater.* **2014**, 13, 139.
- [29] X. M. Li, M. H. Bi, L. Cui, Y. Z. Zhou, X. W. Du, S. Z. Qiao, J. Yang, *Adv. Funct. Mater.* **2017**, 27, 9.
- [30] M. W. Knight, N. S. King, L. F. Liu, H. O. Everitt, P. Nordlander, N. J. Halas, *ACS Nano* **2014**, 8, 834.
- [31] H. P. Liu, T. Z. Liu, L. Zhang, L. Han, C. B. Gao, Y. D. Yin, *Adv. Funct. Mater.* **2015**, 25, 5435.
- [32] M. Losurdo, I. Bergmair, B. Dastmalchi, T. H. Kim, M. M. Giangregorio, W. Y. Jiao, G. V. Bianco, A. S. Brown, K. Hingerl, G. Bruno, *Adv. Funct. Mater.* **2014**, 24, 1864.
- [33] M. M. Shahjamali, Y. Zhou, N. Zareae, C. Xue, J. Wu, N. Large, C. M. McGuirk, F. Boey, V. Dravid, Z. Cui, G. C. Schatz, C. A. Mirkin, *ACS Nano* **2016**, 10, 5362.
- [34] W. T. Lu, S. Sridhar, *Phys. Rev. B* **2008**, 77, 4.
- [35] L. Li, L. Sun, J. Sebastian Gomez-Diaz, N. L. Hogan, P. Lu, F. Khatkhatay, W. Zhang, J. Jian, J. Huang, Q. Su, M. Fan, C. Jacob, J. Li, X. Zhang, Q. Jia, M. Sheldon, A. Alù, X. Li, H. Wang, *Nano Lett.* **2016**, 16, 3936.
- [36] M. S. Rill, C. Plet, M. Thiel, I. Staude, G. Von Freymann, S. Linden, M. Wegener, *Nat. Mater.* **2008**, 7, 543.
- [37] J. J. Huang, X. Wang, N. L. Hogan, S. Wu, P. Lu, Z. Fan, Y. Dai, B. Zeng, R. Starko-Bowes, J. Jian, H. Wang, L. Li, R. P. Prasankumar, D. Yarotski, M. Sheldon, H.-T. Chen, Z. Jacob, X. Zhang, H. Wang, *Adv. Sci.* **2018**, 5, 1800416.
- [38] Y. J. Liu, H. Y. Chu, Y. P. Zhao, *J. Phys. Chem. C* **2010**, 114, 8176.
- [39] D. X. Ye, Y. P. Zhao, G. R. Yang, Y. G. Zhao, G. C. Wang, T. M. Lu, *Nanotechnology* **2002**, 13, 615.
- [40] M. Ohring, *Materials Science of Thin Films*, Academic Press, San Diego, CA, USA **2001**.
- [41] L. Vitos, A. V. Ruban, H. L. Skriver, J. Kollar, *Surf. Sci.* **1998**, 411, 186.
- [42] F. Che, S. Grabtchak, W. M. Whelan, S. A. Ponomarenko, M. Cada, *Results Phys.* **2017**, 7, 593.
- [43] H. Tian, Z. G. Zhou, T. R. Liu, C. Karina, U. Guler, V. Shalaev, P. Bermel, *Appl. Phys. Lett.* **2017**, 110, 5.
- [44] A. D. Rakic, A. B. Djuricic, J. M. Elazar, M. L. Majewski, *Appl. Opt.* **1998**, 37, 5271.